



Contents lists available at ScienceDirect

Materials & Design

journal homepage: www.elsevier.com/locate/matdes

Tuning of structure, grain orientation and mechanical properties in reactively sputtered (Al,Mo,Ta,V,W)N



Andreas Kretschmer^{a,*}, Tomasz Wojcik^a, Roman Schuster^{a,b}, Kumar Yalamanchili^c, Helmut Rudigier^{c,d}, Paul Heinz Mayrhofer^a

^aInstitute of Materials Science and Technology, TU Wien, Getreidemarkt 9, 1060 Vienna, Austria

^bChristian Doppler Laboratory for Interfaces and Precipitation Engineering (CDL-IPE), Institute of Materials Science and Technology, TU Wien, Getreidemarkt 9, 1060 Vienna, Austria

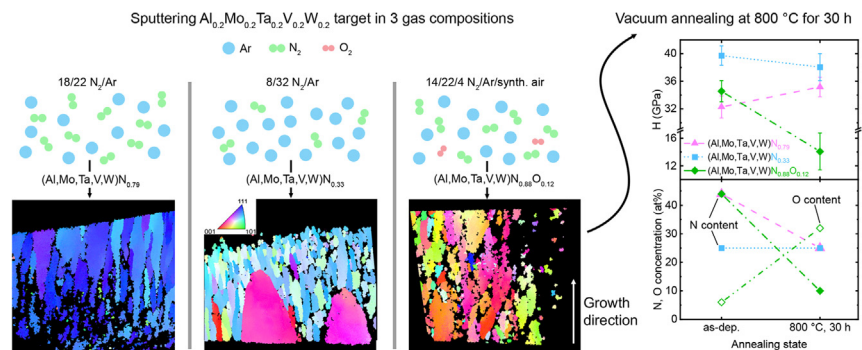
^cOerlikon Balzers, Oerlikon Surface Solutions AG, Iramalli 18, 9496 Balzers, Liechtenstein

^dOC Oerlikon Management AG, 8808 Pfäffikon SZ, Switzerland

HIGHLIGHTS

- (Al,Mo,Ta,V,W)N_{0.79} and -N_{0.33} show columnar microstructures.
- The oxynitride features a renucleated finer, randomly oriented microstructure.
- N-deficiency of (Al,Mo,Ta,V,W)N is beneficial for hardness and phase stability.
- The oxynitride is harder than the N-rich nitride in as-deposited state.
- The oxynitride cracks open during annealing due to formation of binary oxides.

GRAPHICAL ABSTRACT



ARTICLE INFO

Article history:

Received 5 August 2021

Revised 3 December 2021

Accepted 21 December 2021

Available online 22 December 2021

Keywords:

PVD

High-entropy nitrides

Vacancies

Microstructure

ABSTRACT

(Al,Mo,Ta,V,W)-N_{0.79}, -N_{0.33}, and -N_{0.88}O_{0.12} coatings were sputtered in N₂-rich, N₂-lean, and N₂+O₂-containing atmospheres. The face-centered cubic structured coatings feature as-deposited hardness values of 32.3, 39.7, and 34.5 GPa, respectively. The (Al,Mo,Ta,V,W)N_{0.79} and (Al,Mo,Ta,V,W)N_{0.33} consist of highly oriented columns, plus some very large grains in the latter coating. During vacuum annealing at 800 °C for 30 h, the (Al,Mo,Ta,V,W)N_{0.79} loses N down to 25 at.%, while the (Al,Mo,Ta,V,W)N_{0.33} remains stable. Their alignment in chemical composition also caused an approach of their hardness values with 35.2 and 38.1 GPa, respectively. The (Al,Mo,Ta,V,W)N_{0.88}O_{0.12} exhibits partly tilted and randomly oriented smaller columnar grains than the nitrides, and the hardness drops from 34.5 to only 14.1 GPa when vacuum annealed due to massive phase-transformations toward individual oxides and the connected crack formation.

© 2021 The Authors. Published by Elsevier Ltd. This is an open access article under the CC BY license (<http://creativecommons.org/licenses/by/4.0/>).

1. Introduction

High-entropy sublattice ceramics (HESC) – a subset within the high-entropy materials, discovered in 2004 [1,2] – gain increasing recognition and attention [3]. They are characterized by disordered single-phase solid solutions of at least five elements in equiatomic or near-equiatomic composition, resulting in a high configurational entropy $S_{config} \geq 1.5 \cdot R$, with R being the universal gas constant.

* Corresponding author.

E-mail addresses: Andreas.Kretschmer@tuwien.ac.at (A. Kretschmer), Tomasz.Wojcik@tuwien.ac.at (T. Wojcik), Roman.Schuster@tuwien.ac.at (R. Schuster), Kumar.Yalamanchili@oerlikon.com (K. Yalamanchili), Helmut.Rudigier@oerlikon.com (H. Rudigier), Paul.Mayrhofer@tuwien.ac.at (P.H. Mayrhofer).

High-entropy materials benefit from the four so-called core-effects: High configurational entropy, severe lattice distortion, sluggish diffusion, and the cocktail-effect [4]. To distinguish high-entropy materials from lower-entropy counterparts, two definitions have been formulated, a composition-based definition and an entropy-based definition [5]. The entropy-based definition is more concise, and has been specified more precisely for high-entropy ceramics which are composed of a metal sublattice and a non-metal sublattice. Since usually only the metal-sublattice is occupied by five or more different elements, while the non-metal sublattice is rarely modified, the entropy criterion $S_{config} \geq 1.5 \cdot R$ is only reached for one sublattice and thus only per formula unit rather than per atom. To reflect this, the term HESC has been coined [6].

Among the different ceramic classes, physical vapor deposited (PVD) transition metal nitrides offer a combination of properties useful for protective coatings. High-entropy sublattice nitrides (HESN) can be synthesized easily with reactive sputtering techniques and are reported to possess good thermal stability [6,7], mechanical [8,9] and tribological properties [10,11], and oxidation resistance [12–14].

The microstructure and mechanical properties of reactively sputtered HESN depend strongly on the N_2 partial pressure used during deposition. For most coatings a hardness increase with rising N-content due to increased metal-N bonding is reported, which typically maxes out at $\geq 40\text{at}\% \text{ N}$ when approaching the 1:1 stoichiometry of the fcc B1 structure (NaCl prototype) [15–17]. But in some cases, the hardness peak is reached at intermediate N contents, whereas more N incorporation leads to either no change [18–20] or a slight decrease in hardness [9]. This was explained with a saturation of covalent bonds above a certain N concentration and to different microstructures, whose formation depend on the sputter conditions.

Another approach to modify the mechanical properties is the deposition of oxynitride coatings. Cr and Al [21–23], Ta [24], or Zr [25] based PVD oxynitride coatings with good tribological properties have been reported, but data on high-entropy oxynitrides is still sparse [26].

To study the impact of different non-metal sublattice occupations, we modified and compared the microstructure, thermal, and mechanical properties of reactively magnetron sputtered (Al, Mo, Ta, V, W)N by depositing coatings with high or low N_2 partial pressure, and by depositing an oxynitride coating of the same metals. An important difference to the materials mentioned in the last paragraphs is the tendency of most of the constituting metals, Al, Ti, Zr, Hf, and Cr, to form stable fcc nitrides with a 1:1 stoichiometry at room temperature. In (Al, Mo, Ta, V, W)N on the other hand, all the constituting metals except for Al are reported to either prefer N-vacancies in their fcc structure, Mo [27,28], Ta [29,28], and W [30,31], or form N-depleted phases [6]. We can therefore expect weaker Metal-N bonds as a baseline that affect the thermal and mechanical properties.

2. Experimental Details

2.1. Deposition process

All coatings were reactively magnetron sputtered in a modified Leybold Heraeus Z400 magnetron sputtering system, using a powder metallurgically prepared equimolar Al, Mo, Ta, V, and W target of 75 mm in diameter (Plansee Composite Materials GmbH). The coatings were deposited on (1 0 0)-oriented Si ($20 \times 7 \times 0.38\text{mm}^3$), austenitic steel platelets ($20 \times 7 \times 1\text{mm}^3$), and (1 $\bar{1}$ 0 2)-oriented sapphire ($10 \times 10 \times 0.53\text{mm}^3$) substrates, mounted face-to-face to the target at a distance of 4 cm. The depo-

sitions were carried out after reaching a base pressure of 0.3 mPa, the deposition temperature was 440°C and the DC bias potential was set to -50V . Before deposition, the substrates were Ar-ion etched at a pressure of 1.3 Pa for 15 min by applying a negative pulsed DC substrate potential of -150V with a pulse frequency of 150 kHz and a pulse duration of 2496 ns to the substrates.

After pre-sputtering behind the closed shutter for 2 min, the depositions were carried out by supplying a constant current of 0.75 A to the target for 20 min. Three different gas mixtures were used: $N_2/\text{Ar} = 18/22$ and $8/32$ and $N_2/\text{Ar}/\text{synthetic air}$ (20 % O_2 , 80 % N_2) = $14/22/4$ (in sccm). All gases were 99.999 % pure, the deposition pressure was set to 0.44 Pa. The respective power densities on the target in the different gas mixtures were 11.2, 10.3, and $11.5 \text{ W}/\text{cm}^2$.

2.2. Sample Analysis

Cross-sections of the coatings on Si and steel substrates were analyzed with a FEI Quanta 250 scanning electron microscope (SEM) - equipped with a field emission gun (FEG) and operated at 5 kV - to investigate growth morphology and deposition rates. Transmission electron microscopy (TEM) was performed on as-deposited samples with a FEI TECNAI F20, equipped with a FEG, operated at 200 kV. Transmission Kikuchi Diffraction (TKD) patterns were recorded in the FEI quanta 250 with an EDAX Hikari EBSD system on prepared TEM-samples at a working distance of 5 mm and tilting angle of 30° with 30 kV acceleration voltage to study grain orientation. TiN in rock-salt structure (space group $Fm\bar{3}m$) was chosen as structure prototype. The TKD datasets were collected on hexagonal grids with a step size of 10 nm for the nitride samples and 15 nm for the oxynitride. The datasets were processed and analyzed with the EDAX OIM analysis software v8.0. Data clean-up was performed by using the confidence index (CI) standardization procedure, where the CI of each data point is set to the maximum value in the grain, where grains are defined with a misorientation tolerance of 5° . Secondly, one step of the neighbor orientation correlation procedure was performed, where the orientation of single data points, surrounded by at least 4 nearest neighbors belonging to the same grain, was changed to the orientation of the corresponding grain. Finally, a single iteration of grain dilation was performed to close the gaps between adjacent grains. For the data analysis, only data points with a $CI \geq 0.1$ were used. The Matlab Toolbox MTEX version 6.6.1 [32] was used to calculate the orientation distribution functions and the misorientation distribution functions.

Chemical compositions of as-deposited and annealed coatings were analyzed by energy dispersive X-ray spectroscopy (EDS). Phase analysis was conducted with X-ray-diffraction (XRD) using a PANalytical XPert Pro MPD ($\theta - \theta$ diffractometer) using a $\text{Cu-K}\alpha$ source ($\lambda = 0.15408 \text{ nm}$, 45 kV and 40 mA) in Bragg-Brentano geometry. Coatings on sapphire substrates were vacuum annealed in a Centorr LF22-2000 vacuum furnace at $T_a = 800^\circ\text{C}$ for 30 h, the heating rate was 20 K/min, and the passive cooling rate at least 50 K/min down to 200 °C.

Indentation hardness, H , and indentation modulus, E , were measured on coated sapphire substrates with an UMIS II nanoindenter, following the procedure by Oliver and Pharr [33] to analyze the load-displacement curves.

3. Results and Discussion

3.1. Chemistry and Growth morphology

Table 1 shows the chemical compositions of all coatings in as-deposited state and after annealing to 800 °C for 30 h. The metal

Table 1

Chemical Analysis in at.% measured by EDS on samples in as-deposited and annealed state. The given statistical uncertainties are standard deviations of three measurements across a sample.

$f_{N_2/Ar/synth.air}$		Al	Mo	Ta	V	W	N	O
18/22/-	as-dep.	6 ± 1	12 ± 1	13 ± 1	12 ± 1	13 ± 1	44 ± 1	-
18/22/-	annealed	10 ± 1	18 ± 1	15 ± 1	16 ± 1	16 ± 1	25 ± 2	-
8/32/-	as-dep.	9 ± 1	16 ± 1	18 ± 1	15 ± 1	17 ± 1	25 ± 3	-
8/32/-	annealed	9 ± 1	16 ± 1	18 ± 1	15 ± 1	17 ± 1	25 ± 3	-
14/22/4	as-dep.	7 ± 1	10 ± 1	11 ± 1	11 ± 1	11 ± 1	44 ± 5	6 ± 1
14/22/4	annealed	8 ± 1	11 ± 1	13 ± 1	12 ± 1	14 ± 1	10 ± 2	32 ± 2

ratios are very similar between the coatings, with the exception of Al, which shows an increased concentration in the oxynitride. All coatings are understoichiometric - the degree depending on the N_2 partial pressure - due to the tendency to form N-vacancies in the nitrides of Mo [34,35], Ta [36,37] (also metal-vacancies are reported), V [38,6], and W [39,40].

The coatings deposited with gas flow ratios of $N_2/Ar = 18/22$ and $8/32$ sccm will be denoted throughout the article as (Al,Mo,Ta,V,W) $N_{0.79}$ and (Al,Mo,Ta,V,W) $N_{0.33}$, respectively, and the oxynitride coating as (Al,Mo,Ta,V,W) $N_{0.88}O_{0.12}$.

Fig. 1 shows the fracture and polished cross-sections of the three deposited coatings, observed in the SEM. Since the (Al,Mo,Ta,V,W) $N_{0.33}$ coating developed cracks on the Si substrate (but not on the other substrates), no clean fracture cross-section of the whole coating thickness could be recorded. But the observed growth morphology is similar to the (Al,Mo,Ta,V,W) $N_{0.79}$ in a), therefore a polished cross-section is shown in b) instead to demonstrate the coating thickness. All three coatings show a dense columnar structure, but the morphology differs slightly between the nitride and the oxynitride. While the (Al,Mo,Ta,V,W) $N_{0.79}$ and (Al,Mo,Ta,V,W) $N_{0.33}$ coatings consist of rather long, straight columns, the (Al,Mo,Ta,V,W) $N_{0.88}O_{0.12}$, Fig. 1c), shows more rounded features. This becomes more apparent in the TEM studies below. The deposition rates are 171, 158, and 148 nm/min, for the (Al,Mo,Ta,V,W) $N_{0.79}$, (Al,Mo,Ta,V,W) $N_{0.33}$, and (Al,Mo,Ta,V,W) $N_{0.88}O_{0.12}$, respectively.

3.2. Microstructure and Orientation

Detailed TEM studies confirm the columnar structure of our coatings. The bright-field (BF) image, Fig. 2a), shows the competitive growth morphology (close to the substrate) leading to dense long columns of the (Al,Mo,Ta,V,W) $N_{0.79}$ coating. The selected area electron diffraction (SAED) pattern, recorded from the encircled area, shows only few spots, Fig. 2b), although governed across

several grains and columns. This indicates a highly oriented film growth. The circles show the reference positions of an fcc lattice with $a = 4.28\text{\AA}$ as would be expected from a polycrystalline sample without texture. The high orientation and uniformity is also visible in the dark field (DF) image, Fig. 2c), where the majority of the crystals are visible under the same beam conditions. The detailed BF recording, Fig. 2d), shows the high defect density of the crystals.

The N-lean (Al,Mo,Ta,V,W) $N_{0.33}$ features a very different grain structure, see the BF-TEM image Fig. 3a). Similar to the (Al,Mo,Ta,V,W) $N_{0.79}$, the majority of the coating consists of around 100 nm-wide columns, but here these are much shorter. In addition, two abnormally large conically shaped grains (outlined by dotted white lines) with a base width of $\approx 1.2\mu\text{m}$ also developed from the substrate. SAED patterns collected from regions (green dashed circles) next to such a large grain (I), and from within the grain (II), yield fcc structures with identical lattice parameters of $\approx 4.27\text{\AA}$ in both cases (within error of measurement). In addition, an EDS line scan across a region with smaller grains and a large grain reveals no significant difference in chemical composition, since the decrease in N signal stems from the varying sample thickness (other metals than Al are omitted in this display for better visibility). Region (I) exhibits more individual diffraction peaks in the SAED, indicating a more random orientation when compared with Fig. 2, but it is still a highly oriented film. Next to some diffraction spots, twin spots mark a second phase with the same symmetry but slightly different lattice parameter, which indicates a second phase with slightly different N occupation, likely attributable to a Mo_2N type phase. A magnified view of the central large grain visible in Fig. 3a) is presented in Fig. 3b) with a high-resolution (HR) image outlining the grain boundary in Fig. 3c). Due to the crystal structure examined by SAED, the chemistry measured by EDS-linescan, and the dense grain boundary region evaluated by HR-TEM we can definitely exclude these large grains to be a macro-particle or generated thereof. The DF image in Fig. 3d) shows that the crystalline

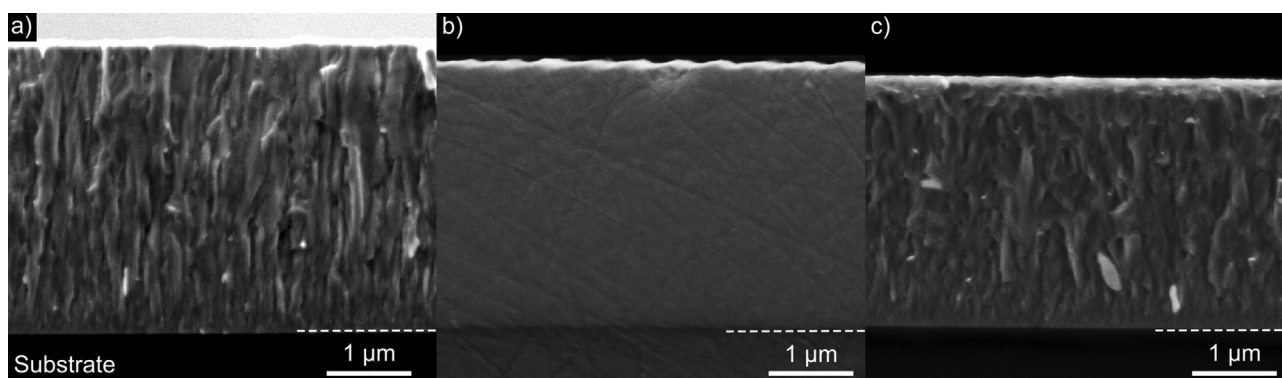


Fig. 1. SEM fracture and polished cross-sections of coatings deposited with different gas flows: a) (Al,Mo,Ta,V,W) $N_{0.79}$, b) (Al,Mo,Ta,V,W) $N_{0.33}$, and c) (Al,Mo,Ta,V,W) $N_{0.88}O_{0.12}$. Due to cracking on the Si substrate, no whole fracture cross-section of the (Al,Mo,Ta,V,W) $N_{0.33}$ could be recorded. Since the fracture cross-section looks very similar to the (Al,Mo,Ta,V,W) $N_{0.79}$, a polished cross-section is presented instead to show the deposition rate.

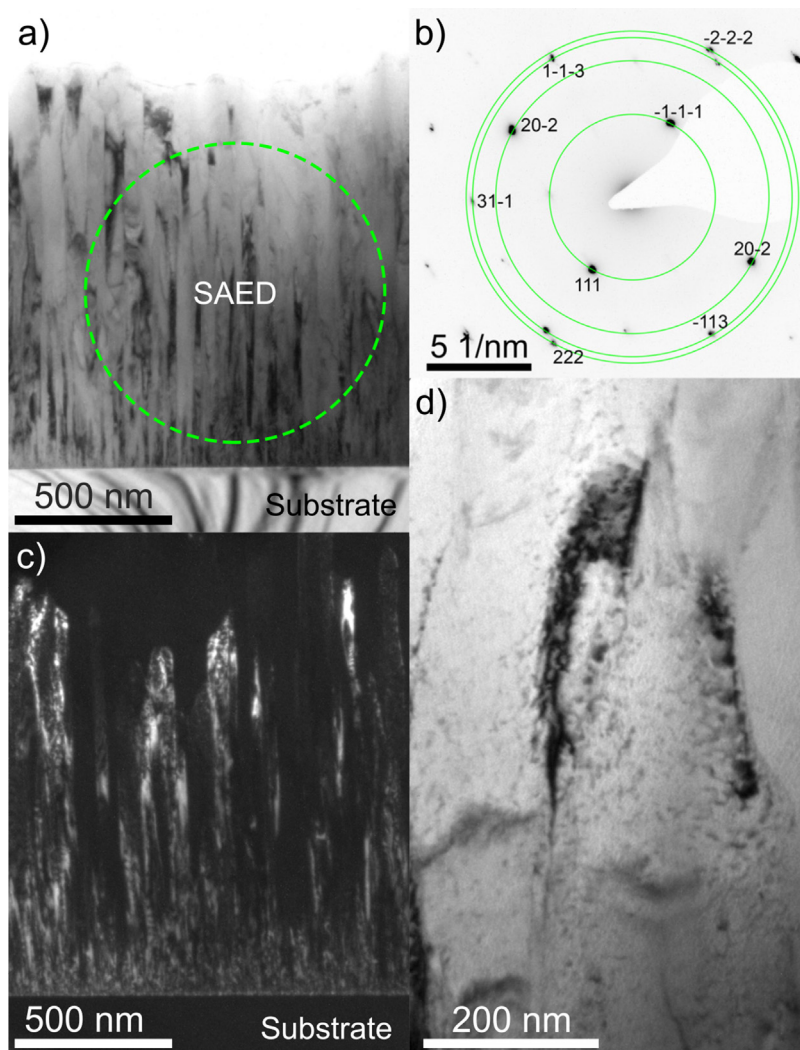


Fig. 2. TEM images of the $(\text{Al,Mo,Ta,V,W})\text{N}_{0.79}$ coating: a) Bright field image, b) SAED pattern of the circled area in a), c) dark field image, d) bright field magnification of columns.

columns are distinctly shorter than in the $(\text{Al,Mo,Ta,V,W})\text{N}_{0.79}$ coating.

TEM investigations of the oxynitride coating $(\text{Al,Mo,Ta,V,W})\text{N}_{0.88}\text{O}_{0.12}$ yield a dense coating, that features V-shaped grains at an angle of $\approx 20^\circ$ to the growth direction instead of straight columns, Fig. 4a). On top of the coating some Cu-redeposition from the TEM sample preparation can be seen. Overall, the growth morphology does not show the typical competitive growth close to the substrate as for $(\text{Al,Mo,Ta,V,W})\text{N}_{0.79}$ and $(\text{Al,Mo,Ta,V,W})\text{N}_{0.33}$. The SAED taken from the region indicated with a circle shows a single fcc phase, Fig. 4b). The slight presence of ring patterns indicates a much less oriented growth than for the nitrides, likely facilitated by the tilted growth. The lattice parameter calculated from the fcc diffraction spots is $\approx 4.28\text{\AA}$. Fig. 4c) is the DF version of Fig. 4a), highlighting the partly tilted growth of individual grains. The very dense growth morphology and high defect density is visible in the higher magnification investigation, Fig. 4d), of the region marked with a dashed square in Fig. 4a).

To analyze the influence of the deposition atmosphere during growth and the resulting film composition on the developing film microstructures in more detail, the TEM samples were investigated by Transmission Kikuchi Diffraction. The inverse pole figure maps, pole figures, and misorientation angle and axis distribution plots

are shown for $(\text{Al,Mo,Ta,V,W})\text{N}_{0.79}$ in Fig. 5a), for $(\text{Al,Mo,Ta,V,W})\text{N}_{0.33}$ in Fig. 5f), and for $(\text{Al,Mo,Ta,V,W})\text{N}_{0.88}\text{O}_{0.12}$ in Fig. 5g), respectively.

The $(\text{Al,Mo,Ta,V,W})\text{N}_{0.79}$ shows a strong orientation relationship between substrate and coating, (Fig. 5a). The grains, which in some cases stretch from the substrate all the way through the coating, can be divided in two orientation groups. The dominant misorientation axis between the two orientations is the $[1\ 1\ 0]$ axis, the second axis is oriented along the $[1\ 1\ 1]$ direction. The $[1\ 1\ 0]$ pole in Fig. 5b) is oriented close to the growth direction and aligns well with $[0\ 1\ \bar{1}\ 1]$ pole of the sapphire substrate (black crosses), which is therefore the dominant rotation axis since it runs through the mostly vertical grain boundaries. The misorientation angle distribution is also divided in two groups with small angles $\approx 5^\circ$ (between the grains of one orientation group) and $\approx 60^\circ$ between the grains of different orientation groups (Fig. 5c). The angular distribution for a uniform cubic grain orientation is shown for comparison and highlights the strong texture once again. The misorientation axis distribution plot also exemplifies the strong $[1\ 1\ 0]$ and $[1\ 1\ 1]$ orientation.

Like in the TEM investigations, we see a distinctly different microstructure in $(\text{Al,Mo,Ta,V,W})\text{N}_{0.33}$ compared to the N-rich coating, see Fig. 5d). Next to two very big grains with similar

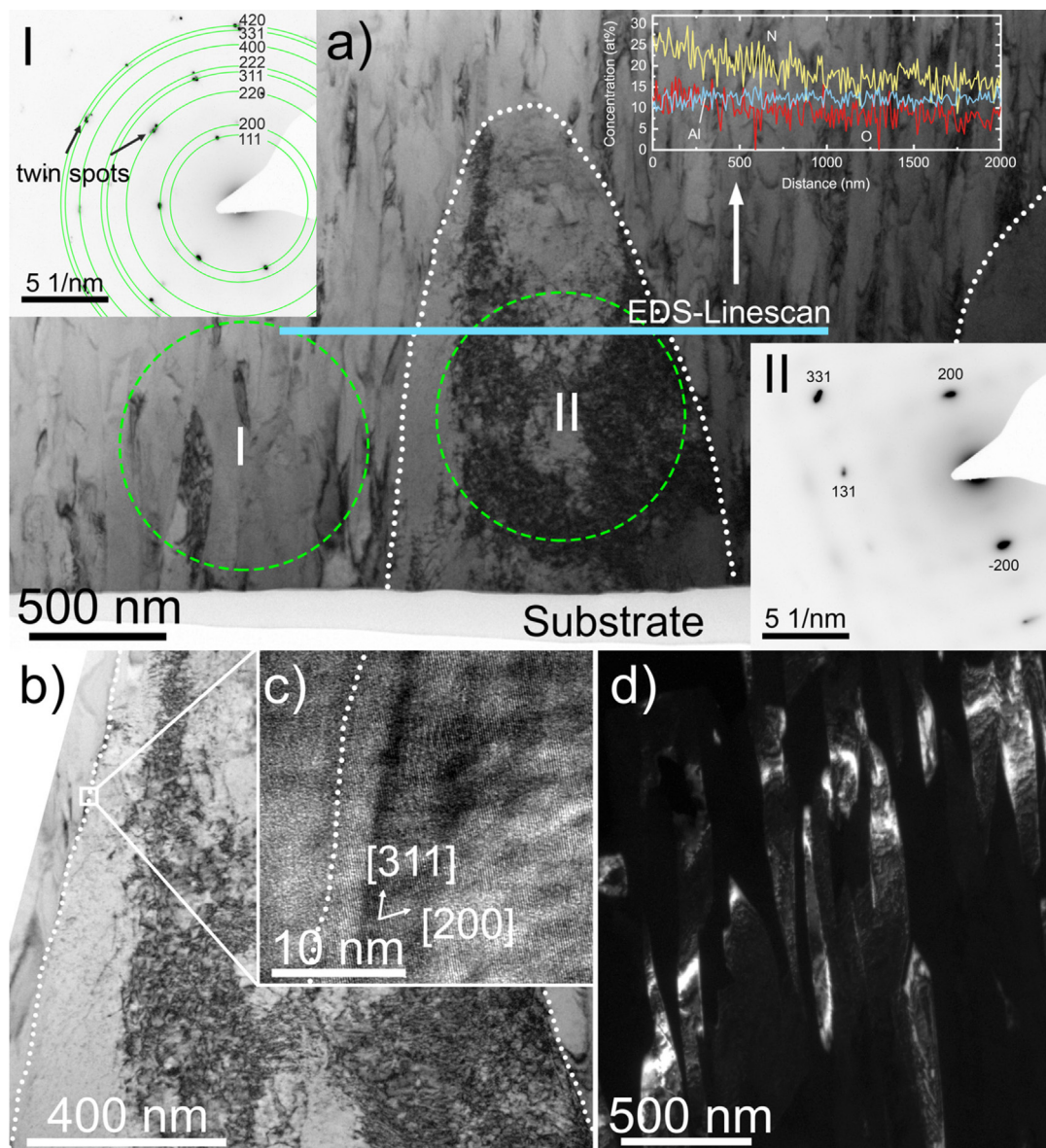


Fig. 3. TEM images of the (Al,Mo,Ta,V,W)N_{0.33} coating: a) Bright field image, with two SAED patterns recorded from the circles I and II, abnormally large grains are outlined with dots. An EDS-Linescan across one such grain shows a constant chemical composition between these regions. Other elemental lines are omitted for better visibility. b) magnified view of the central large grain in a), c) high-resolution image at the border region of the large grain in b), d) dark field image of the columnar region next to the large grains.

orientation many smaller and shorter columnar grains make up the coating. Within these smaller grains we see again a division into two groups like in the (Al,Mo,Ta,V,W)N_{0.79}. The coating features a strong [1 1 0] pole in vertical direction similar to the (Al,Mo,Ta,V,W)N_{0.79}, but the grain orientation is slightly twisted, compare Fig. 5d), likely due to sample preparation. The orientation relationship to the substrate is also disturbed since the [0 1 $\bar{1}$ 1] pole (black cross in Fig. 5e) of the sapphire substrate does not match the column orientation as well. Instead, the crystallographically less important pole [2 $\bar{2}$ 0 1] (+ in Fig. 5e) lies closer to the grain orientation. The texture is therefore less dependent from the substrate, and less pronounced as for (Al,Mo,Ta,V,W)N_{0.79}. In the misorientation angle distribution plot, Fig. 5f), we see a comparable distribution as in Fig. 5c), with an additional contribution at $\approx 35^\circ$ due to the large grains. This also results in the wider misorientation axis distribution between the [1 1 0] and [1 1 1] poles compared to the (Al,Mo,Ta,V,W)N_{0.79} in Fig. 5c).

The (Al,Mo,Ta,V,W)N_{0.88}O_{0.12} shows the most randomized grain orientation (Fig. 5g). The grains are occasionally columnar and partly smaller equiaxed. Some of the columns are aligned in growth direction, while others are tilted by $\approx 20^\circ$ to the growth direction. The most pronounced texture in growth direction is the [1 0 0], but the coating consists of many other randomly oriented small grains as well, so that the pole figures, Fig. 5h), do not show a clear pattern. The misorientation angle distribution as well as the misorientation axis distribution, Fig. 5i), follow the purely random orientation closely except for small angles, which are over represented in the coating.

3.3. Thermal stability and mechanical properties

The XRD patterns of the coatings in as-deposited state, Fig. 6a), and after annealing to 800 °C for 30 h, Fig. 6b), confirm the phase analysis by SAED. The as-deposited (Al,Mo,Ta,V,W)N_{0.79} coating is

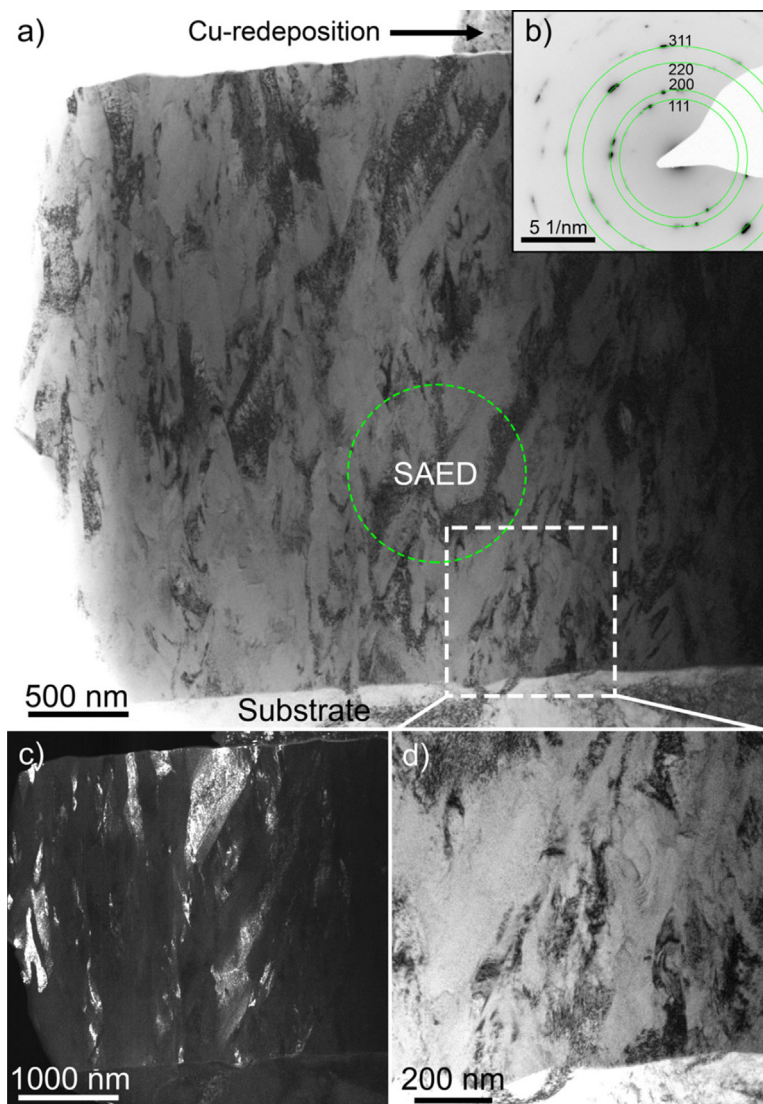


Fig. 4. TEM images of the $(\text{Al,Mo,Ta,V,W})\text{N}_{0.88}\text{O}_{0.12}$ coating: a) Bright-field image, b) SAED pattern collected from the circled region in a), c) dark field image, d) magnified bright field image of the substrate near region outlined in a).

highly (2 0 0) oriented. After annealing, this highly preferred orientation remains, but the peak shifts to higher diffraction angles (please use the TiN standard positions as a reference). The lattice parameter shrinks accordingly from 4.27 to 4.20 Å. At the same time the full width at half maximum of the (2 0 0) peak increases from 0.54 to 0.89°. Thus, while the macrostresses might decrease due to the annealing treatment, the microstresses remain or even increase. An additional cause for the peak shift and decreased lattice parameter can be the N-loss, as detected by EDS. After annealing, this coating (starting as $(\text{Al,Mo,Ta,V,W})\text{N}_{0.79}$) has approximately the same N-content of 25 at.% as $(\text{Al,Mo,Ta,V,W})\text{N}_{0.33}$ (Table 1), which was prepared with a N_2/Ar ratio of only 8/32. With increasing N-vacancy concentration the lattice parameters of MoN_x [41,42], Ta_xN_x [43,28], and WN_x [40,44] shrink, as suggested by DFT calculations. The additional XRD features at $\approx 60^\circ$ and $\approx 68^\circ$ indicate the formation of a hexagonal Ta_2N -based phase and are thus early signs for a decomposition. This will also contribute to the increased peak broadening.

The $(\text{Al,Mo,Ta,V,W})\text{N}_{0.33}$ coating is also predominantly (2 0 0) oriented, but a small (3 1 1) reflex is also present in as-deposited state. Remarkably, the relative shift of the peaks to the reference

positions of TiN is different for the (2 0 0) peak (shifted to lower angles), than for the (3 1 1) peak (shifted to higher angles), indicating slightly different phases, which agrees well with the SAED analysis. When estimating the lattice parameter from the peak positions, we get $a = 4.28\text{Å}$ using the (2 0 0) peak, and $a = 4.21 \pm 0.02\text{Å}$ using the (3 1 1) peak, which is close to the lattice parameter of Mo_2N [28]. Since the total N content of this sample, as estimated by EDS (Table 1), is only about 25 at.%, both phases must exhibit high N-vacancy concentrations. After annealing, the (3 1 1) peak can not be detected anymore, but the (2 0 0) reflex developed a pronounced left-hand shoulder. The lattice parameter, estimated from the (2 0 0) peak position, stays at 4.28Å, and also the chemical composition is unchanged from the as-deposited value within the error of measurement, indicating a chemical equilibrium composition for this coating.

The $(\text{Al,Mo,Ta,V,W})\text{N}_{0.88}\text{O}_{0.12}$ coating exhibits a random growth orientation with clearly visible (1 1 1), (2 0 0), (2 2 0), (3 1 1), and (2 2 2) reflexes. But also this coating is clearly single-phased fcc-structured in its as-deposited state. This changes fundamentally during annealing, during which the N content decreases from 44 to 9 at.% and the O content increases from 6 to 32 at.% (Table 1).

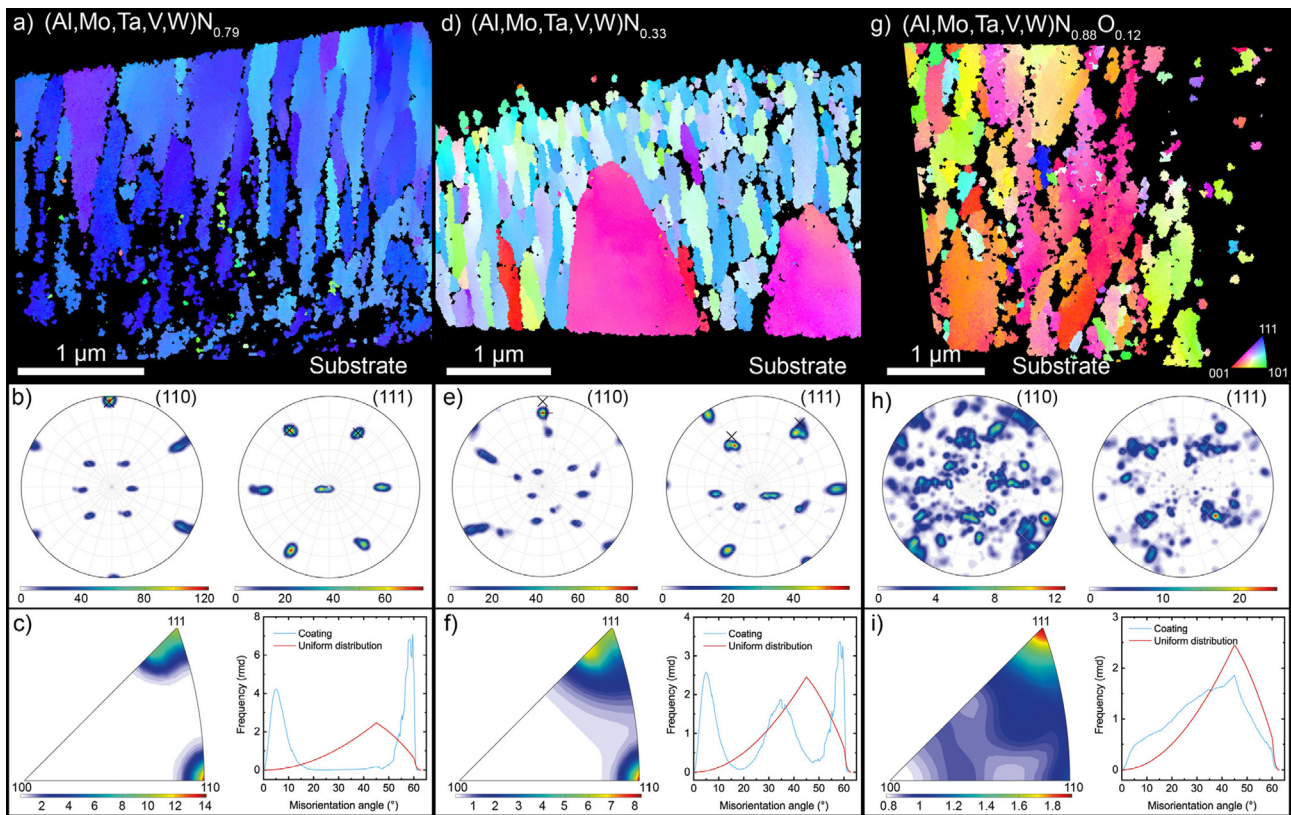


Fig. 5. Inverse pole figures maps, pole figures, and misorientation axis distribution and misorientation angle distribution plots, measured by TKD of $(\text{Al,Mo,Ta,V,W})\text{N}_{0.79}$ in a), b), and c), of $(\text{Al,Mo,Ta,V,W})\text{N}_{0.33}$ in d), e), and f), and of $(\text{Al,Mo,Ta,V,W})\text{N}_{0.88}\text{O}_{0.12}$ in g), h), and i), respectively (all coatings as-deposited). Black crosses in the pole figures mark the $[0\ 1\ \bar{1}\ 1]$ pole, and + the $[2\ \bar{2}\ 0\ 1]$ pole of the substrate.

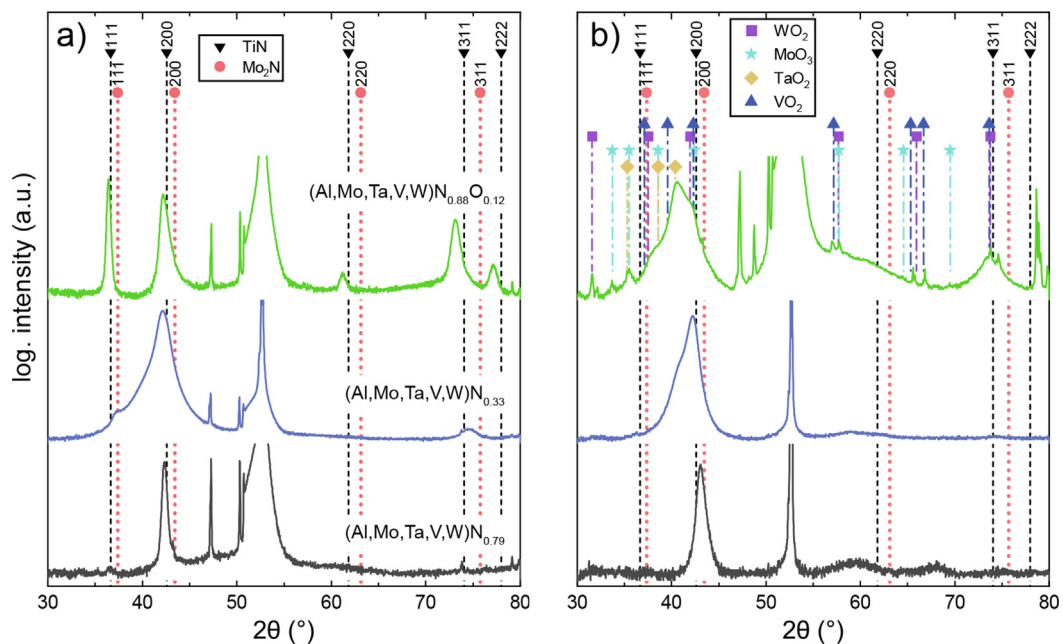


Fig. 6. XRD patterns of coatings in as-deposited state a) and after annealing at 800°C for 30h b).

After the 30 h annealing at 800 °C, the XRD pattern shows the presence of W, Mo, Ta, and V oxides. A corresponding decomposition was also observed in (Co,Cr,Fe,Mn,Ni) -oxynitride films [26]. Since the specific volumes of the oxides are much larger than of the oxynitride phase (12.3, 11.3, 9.9, and 11.1 Å³/at for MoO₃ [45],

TaO₂ [46], VO₂ [47], and WO₂ [48], respectively, versus 9.8 Å³/at in the $(\text{Al,Mo,Ta,V,W})\text{N}_{0.88}\text{O}_{0.12}$ coating) this phase separation causes the coating to crack open, as proven by SEM top-view investigations, Fig. 7. The as-deposited and annealed state of the $(\text{Al,Mo,Ta,V,W})\text{N}_{0.79}$, $(\text{Al,Mo,Ta,V,W})\text{N}_{0.33}$, and $(\text{Al,Mo,Ta,V,W})\text{N}_{0.88}\text{O}_{0.12}$ are

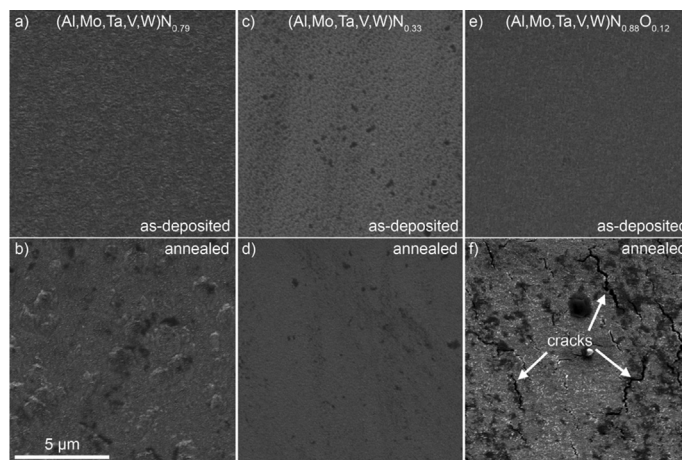


Fig. 7. SEM top-view micrographs show that the surface of the $(\text{Al,Mo,Ta,V,W})\text{N}_{0.79}$ coating stays smooth after annealing at $800\text{ }^{\circ}\text{C}$ for 30 h, except for some island formation a)-b). No change is visible in the surface of the $(\text{Al,Mo,Ta,V,W})\text{N}_{0.33}$ c)-d), while the $(\text{Al,Mo,Ta,V,W})\text{N}_{0.88}\text{O}_{0.12}$ develops cracks due to separation into oxide phases with larger specific volumes e)-f).

compared in Fig. 7a), respectively. All three coatings feature comparably smooth surfaces in as-deposited state. After annealing, coarse features in the order of $\approx 1\text{ }\mu\text{m}$ appear on the $(\text{Al,Mo,Ta,V,W})\text{N}_{0.79}$, which could be a sign of the ongoing decomposition. On the $(\text{Al,Mo,Ta,V,W})\text{N}_{0.33}$, the surface appears to be even smoother after annealing, no other change is visible after annealing. On the $(\text{Al,Mo,Ta,V,W})\text{N}_{0.88}\text{O}_{0.12}$, cracks spanning several μm in length are drawn through the surface with only few μm between the cracks. Thus, the exposed surface area increases greatly, this allows N to leave and O to enter the coating more easily, leading to the complete change in chemistry compared with the as-deposited state.

The indentation hardness H , Fig. 8a), and indentation modulus E , Fig. 8b), of the coatings in their as-deposited state and after the 30 h annealing at $800\text{ }^{\circ}\text{C}$ nicely reflect the microstructural and morphological changes. In the as-deposited state, the $(\text{Al,Mo,Ta,V,W})\text{N}_{0.79}$ coating exhibits a hardness of $32.3 \pm 1.6\text{ GPa}$, which is exceeded by both the $(\text{Al,Mo,Ta,V,W})\text{N}_{0.88}\text{O}_{0.12}$ and $(\text{Al,Mo,Ta,V,W})\text{N}_{0.33}$ coatings with $34.6 \pm 1.5\text{ GPa}$ and $39.7 \pm 1.4\text{ GPa}$, respectively. The latter is even touching the domain of superhard materials (for which the hardness would need to be above 40 GPa [49]). After the annealing treatment, the $(\text{Al,Mo,Ta,V,W})\text{N}_{0.79}$ allows for

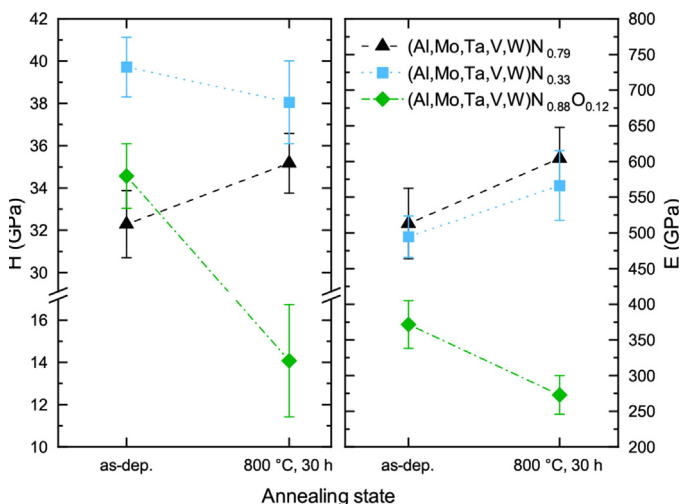


Fig. 8. Hardness H and Indentation modulus E measured on coatings in as-deposited (as-dep.) state and after annealing at $800\text{ }^{\circ}\text{C}$ for 30 h.

even $35.2 \pm 1.4\text{ GPa}$, while the hardness of $(\text{Al,Mo,Ta,V,W})\text{N}_{0.33}$ decreased slightly to $38.1 \pm 2.0\text{ GPa}$. Only the $(\text{Al,Mo,Ta,V,W})\text{N}_{0.88}\text{O}_{0.12}$ suffers a severe hardness loss down to $14.1 \pm 2.7\text{ GPa}$, which can be explained by the almost entire transformation towards individual oxides and the concomitant formation of cracks. But interestingly, the $(\text{Al,Mo,Ta,V,W})\text{N}_{0.79}$ and $(\text{Al,Mo,Ta,V,W})\text{N}_{0.33}$ coatings, which are separated in their hardness by 8 GPa in as-deposited state, exhibit only a difference of $\approx 3\text{ GPa}$ after the annealing treatment. The latter caused also an alignment in their chemical composition, which became almost identical especially with respect to their N-content, although they started with 44 respectively 25 at.% (Table 1). The significantly higher hardness of the N-lean $(\text{Al,Mo,Ta,V,W})\text{N}_{0.33}$, already in its as-deposited state, combined with the annealing-induced hardness increase of the originally N-richer $(\text{Al,Mo,Ta,V,W})\text{N}_{0.79}$, suggests that for this material system – $(\text{Al,Mo,Ta,V,W})\text{N}$ – a N/metal ratio of 1/2 to 1/3 is beneficial in terms of hardness and phase stability. The observed hardness trend nicely follows the decreasing valence electron concentration from $9.2\text{ e}^-/\text{f.u.}$ in the as-deposited $(\text{Al,Mo,Ta,V,W})\text{N}_{0.79}$ to $6.9\text{ e}^-/\text{f.u.}$ in both the annealed $(\text{Al,Mo,Ta,V,W})\text{N}_{0.79}$ and the $(\text{Al,Mo,Ta,V,W})\text{N}_{0.33}$ (as-deposited and annealed) due to the N-vacancies in the fcc structure [42,50,51].

Interestingly, the indentation moduli of $(\text{Al,Mo,Ta,V,W})\text{N}_{0.79}$ and $(\text{Al,Mo,Ta,V,W})\text{N}_{0.33}$ are very similar with $513 \pm 50\text{ GPa}$ and $495 \pm 28\text{ GPa}$ in their as-deposited state as well as after annealing, during which the modulus increased to $604 \pm 44\text{ GPa}$ and $566 \pm 49\text{ GPa}$, respectively. The $(\text{Al,Mo,Ta,V,W})\text{N}_{0.88}\text{O}_{0.12}$ coating, although only containing 6 at.% O exhibits a much lower indentation modulus of only $372 \pm 33\text{ GPa}$ in the as-deposited state, which further decreased to $273 \pm 27\text{ GPa}$ during annealing, as a consequence of the massive structural and chemical changes.

4. Conclusions

The microstructure, mechanical properties, and thermal stability of (Al,Mo,Ta,V,W) -nitrides can be easily modified by the sputter gas composition. Both deposited nitrides, $(\text{Al,Mo,Ta,V,W})\text{N}_{0.79}$ and $(\text{Al,Mo,Ta,V,W})\text{N}_{0.33}$, exhibit significant N-vacancy concentrations, while in the as-deposited oxynitride with 6 at.% O the metal/non-metal ratio is roughly 1. Structurally, the $(\text{Al,Mo,Ta,V,W})\text{N}_{0.79}$ consists of long, highly oriented columns. The $(\text{Al,Mo,Ta,V,W})\text{N}_{0.33}$ is also textured to a lesser extent, but the columns are much shorter. In addition, much larger grains can be found throughout the coating. The $(\text{Al,Mo,Ta,V,W})\text{N}_{0.88}\text{O}_{0.12}$ consists of randomly oriented

columns, of which some are tilted 20° to the growth direction, and smaller equiaxed grains with random growth orientation.

The hardness of the (Al,Mo,Ta,V,W)_{N_{0.79}} is 32.3 GPa in as-deposited state, which increases to 35.2 GPa when vacuum annealed at 800 °C for 30 h. This hardness increase is due to the decreasing N-content from ≈44 to ≈25 at.% with a corresponding decrease in valence electron concentration. The (Al,Mo,Ta,V,W)_{N_{0.33}}, deposited with a lower N₂ partial pressure, does not change its chemistry significantly during annealing and is thus in chemical equilibrium. The hardness also changes only little from 39.7 to 38.1 GPa during annealing. The indentation moduli of both nitride coatings are very similar around 510 and 580 GPa before and after annealing.

The (Al,Mo,Ta,V,W)_{N_{0.88}O_{0.12}} surpasses the hardness of (Al,Mo,Ta,V,W)_{N_{0.79}} with 34.6 GPa in its as-deposited state, which is essentially related to the different microstructure with smaller grains. However, the same annealing treatment as for the nitrides resulted in a severe hardness reduction down to 14.1 GPa due to the transformation towards individual Mo-, Ta-, V-, and W-oxides. Their much higher specific volumes with respect to the starting oxynitride phase causes the coating to crack open.

Data Availability

The raw/processed data required to reproduce these findings cannot be shared at this time as the data also forms part of an ongoing study.

Declaration of Competing Interest

The authors declare that they have no known competing financial interests or personal relationships that could have appeared to influence the work reported in this paper.

Acknowledgements

This work was funded by the Austrian COMET Program (project K2 InTribology, No. 872176). The authors acknowledge the use of the X-ray center (XRC) and USTEM at TU Wien. They are also very grateful to Philip Kutrowatz (TU Wien, Austria) for TEM sample preparation. Plansee Composite Materials GmbH is acknowledged for supplying the target. The authors acknowledge TU Wien Bibliothek for financial support through its Open Access Funding Programme.

References

- [1] J.-W. Yeh, S.-K. Chen, S.-J. Lin, J.-Y. Gan, T.-S. Chin, T.-T. Shun, C.-H. Tsau, S.-Y. Chang, Nanostructured High-Entropy Alloys with Multiple Principal Elements: Novel Alloy Design Concepts and Outcomes, *Adv. Eng. Mater.* 6 (5) (2004) 299–303, <https://doi.org/10.1002/adem.200300567>.
- [2] B. Cantor, I.T. Chang, P. Knight, A.J. Vincent, Microstructural development in equiatomic multicomponent alloys, *Materials Science and Engineering A* 375–377 (1–2 SPEC. ISS.) (2004) 213–218, [doi:10.1016/j.msea.2003.10.257](https://doi.org/10.1016/j.msea.2003.10.257).
- [3] C. Oses, C. Toher, S. Curtarolo, High-entropy ceramics, *Nature Reviews Materials* 5 (4) (2020) 295–309, <https://doi.org/10.1038/s41578-019-0170-8>.
- [4] J.-W. Yeh, *Recent Progress in High-entropy Alloys*, *Annales De Chimie - Science des Matériaux* 31 (2006) 633–648.
- [5] P.H. Mayrhofer, A. Kirnbauer, P. Ertelthaler, C.M. Koller, High-entropy ceramic thin films, A case study on transition metal diborides, *Scripta Materialia* 149 (2018) 93–97, <https://doi.org/10.1016/j.scriptamat.2018.02.008>.
- [6] A. Kirnbauer, A. Kretschmer, C.M. Koller, T. Wojcik, V. Paneta, M. Hans, J.M. Schneider, P. Polcik, P.H. Mayrhofer, Mechanical properties and thermal stability of reactively sputtered multi-principal-metal Hf-Ta-Ti-V-Zr nitrides, *Surf. Coat. Technol.* 389 (2020) 125674, <https://doi.org/10.1016/j.surfcoat.2020.125674>.
- [7] A. Kretschmer, D. Holec, K. Yalamanchili, H. Rudigier, M. Hans, J.M. Schneider, P.H. Mayrhofer, Strain-stabilized Al-containing high-entropy sublattice nitrides, *Acta Mater.* (2021) 117483, <https://doi.org/10.1016/j.actamat.2021.117483>.
- [8] Y.C. Lin, S.Y. Hsu, R.W. Song, W.L. Lo, Y.T. Lai, S.Y. Tsai, J.G. Duh, Improving the hardness of high entropy nitride (Cr_{0.35}Al_{0.25}Nb_{0.12}Si_{0.8}V_{0.20})N coatings via tuning substrate temperature and bias for anti-wear applications, *Surf. Coat. Technol.* 403 (101) (2020) 126417, <https://doi.org/10.1016/j.surfcoat.2020.126417>.
- [9] X. Feng, K. Zhang, Y. Zheng, H. Zhou, Z. Wan, Chemical state, structure and mechanical properties of multi-element (CrTaNbMoV)_{N_x} films by reactive magnetron sputtering, *Mater. Chem. Phys.* 239 (May 2019) (2020) 121991, <https://doi.org/10.1016/j.matchemphys.2019.121991>.
- [10] W.-J. Shen, M.-H. Tsai, J.-W. Yeh, Machining Performance of Sputter-Deposited (Al_{0.34}Cr_{0.22}Nb_{0.11}Si_{0.11}Ti_{0.22})₅₀N₅₀ High-Entropy Nitride Coatings, *Coatings* 5 (3) (2015) 312–325, [doi:10.3390/coatings5030312](https://doi.org/10.3390/coatings5030312).
- [11] A.D. Pogrebnjak, I.V. Yakushchenko, A.A. Bagdasarjan, O.V. Bondar, R. Krause-Rehberg, G. Abadias, P. Chartier, K. Oyoshi, Y. Takeda, V.M. Beresnev, O.V. Sobol, Microstructure, physical and chemical properties of nanostructured (Ti-Hf-Zr-V-Nb)N coatings under different deposition conditions, *Mater. Chem. Phys.* 147 (3) (2014) 1079–1091, <https://doi.org/10.1016/j.matchemphys.2014.06.062>.
- [12] W.-J. Shen, M.-Y. Tsai, K.-Y. Tsai, C.C. Juan, C.W. Tsai, J.W. Yeh, Y.S. Chang, Superior oxidation resistance of (Al_{0.34}Cr_{0.22}Nb_{0.11}Si_{0.11}Ti_{0.22})₅₀N₅₀ high-entropy nitride, *J. Electrochem. Soc.* 160 (11) (2013) 531–535, <https://doi.org/10.1149/2.028311jes>.
- [13] A. Kretschmer, A. Kirnbauer, V. Moraes, D. Primetzhofer, K. Yalamanchili, H. Rudigier, P.H. Mayrhofer, Improving phase stability, hardness, and oxidation resistance of reactively magnetron sputtered (Al, Cr, Nb, Ta, Ti)N thin films by Si-alloying, *Surf. Coat. Technol.* 416 (February) (2021) 127162, <https://doi.org/10.1016/j.surfcoat.2021.127162>.
- [14] J.-J. Wang, F.-Y. Ouyang, Oxidation behavior of Al-Cr-Nb-Si-Zr high entropy nitride thin films at 8507, *Corros. Sci.* 187 (October 2020) (2021) 109467, <https://doi.org/10.1016/j.corsci.2021.109467>.
- [15] K.H. Cheng, C.H. Lai, S.J. Lin, J.W. Yeh, Structural and mechanical properties of multi-element (AlCrMoTaTiZr)_{N_x} coatings by reactive magnetron sputtering, *Thin Solid Films* 519 (10) (2011) 3185–3190, <https://doi.org/10.1016/j.tsf.2010.11.034>.
- [16] R. Chen, Z. Cai, J. Pu, Z. Lu, S. Chen, S. Zheng, C. Zeng, Effects of nitriding on the microstructure and properties of VAlTiCrMo high-entropy alloy coatings by sputtering technique, *J. Alloy. Compd.* 827 (2020) 153836, <https://doi.org/10.1016/j.jallcom.2020.153836>.
- [17] P. Cui, W. Li, P. Liu, K. Zhang, F. Ma, X. Chen, R. Feng, P.K. Liaw, Effects of nitrogen content on microstructures and mechanical properties of (AlCrTiZrHf)N high-entropy alloy nitride films, *J. Alloy. Compd.* 834 (2020) 155063, <https://doi.org/10.1016/j.jallcom.2020.155063>.
- [18] X. Lu, C. Zhang, C. Wang, X. Cao, R. Ma, X. Sui, J. Hao, W. Liu, Investigation of (CrAlTiNbV)_{N_x} high-entropy nitride coatings via tailoring nitrogen flow rate for anti-wear applications in aviation lubricant, *Appl. Surf. Sci.* 557 (March) (2021) 149813, <https://doi.org/10.1016/j.apsusc.2021.149813>.
- [19] H.T. Hsueh, W.J. Shen, M.H. Tsai, J.W. Yeh, Effect of nitrogen content and substrate bias on mechanical and corrosion properties of high-entropy films (AlCrSiTiZr)_{100-x}N_x, *Surf. Coat. Technol.* 206 (19–20) (2012) 4106–4112, <https://doi.org/10.1016/j.surfcoat.2012.03.096>.
- [20] K. von Fieandt, L. Riekehr, B. Osinger, S. Fritze, E. Lewin, Influence of N content on structure and mechanical properties of multi-component Al-Cr-Nb-V-Zr based thin films by reactive magnetron sputtering, *Surf. Coat. Technol.* 389 (March) (2020) 125614, <https://doi.org/10.1016/j.surfcoat.2020.125614>.
- [21] J. Nohava, P. Dessarzin, P. Karvankova, M. Morstein, Characterization of tribological behavior and wear mechanisms of novel oxynitride PVD coatings designed for applications at high temperatures, *Tribol. Int.* 81 (2015) 231–239, <https://doi.org/10.1016/j.triboint.2014.08.016>.
- [22] F. Ahmad, L. Zhang, J. Zheng, I. Sidra, F. Cai, S. Zhang, Structural evolution and high-temperature tribological properties of AlCrON coatings deposited by multi-arc ion plating, *Ceram. Int.* 46 (15) (2020) 24281–24289, <https://doi.org/10.1016/j.ceramint.2020.06.208>.
- [23] K. Bobzin, T. Brögelmann, C. Kalscheuer, M. Naderi, Hybrid dcMS/HPPMS PVD nitride and oxynitride hard coatings for adhesion and abrasion reduction in plastics processing, *Surf. Coat. Technol.* 308 (2016) 349–359, <https://doi.org/10.1016/j.surfcoat.2016.07.103>.
- [24] D. Cristea, D. Constantin, A. Crisan, C.S. Abreu, J.R. Gomes, N.P. Barradas, E. Alves, C. Moura, F. Vaz, L. Cunha, Properties of tantalum oxynitride thin films produced by magnetron sputtering: The influence of processing parameters, *Vacuum* 98 (2013) 63–69, <https://doi.org/10.1016/j.vacuum.2013.03.017>.
- [25] B. Warcholinski, A. Gilewicz, A.S. Kuprin, G.N. Tolmachova, V.D. Ovcharenko, T.A. Kuznetsova, V.A. Lapitskaya, S.A. Chizhik, Comparison of Mechanical and Tribological Properties of Nitride and Oxynitride Coatings Based on Chrome and Zirconium Obtained by Cathodic Arc Evaporation, *Journal of Friction and Wear* 40 (2) (2019) 163–170, <https://doi.org/10.3103/S1068366619020156>.
- [26] D.D. Le, S.K. Hong, T.S. Ngo, J. Lee, Y.C. Park, S.I. Hong, Y.S. Na, Microstructural Investigation of CoCrFeMnNi High Entropy Alloy Oxynitride Films Prepared by Sputtering Using an Air Gas, *Met. Mater. Int.* 24 (6) (2018) 1285–1292, <https://doi.org/10.1007/s12540-018-0143-2>.
- [27] K. Balasubramanian, L. Huang, D. Gall, Phase stability and mechanical properties of Mo_{1-x}N_x with 0 ≤ x ≤ 1, *J. Appl. Phys.* 122 (19) (2017) 12, <https://doi.org/10.1063/1.4998686>.
- [28] N. Koutná, D. Holec, O. Svoboda, F.F. Klimashin, P.H. Mayrhofer, Point defects stabilise cubic Mo-N and Ta-N, *J. Phys. D: Appl. Phys.* 49 (37) (2016) 375303, <https://doi.org/10.1088/0022-3727/49/37/375303>.

- [29] C.M. Koller, A. Kirnbauer, R. Rachbauer, S. Kolozsvári, P.H. Mayrhofer, Thermally-induced phase transformation sequence of arc evaporated Ta-Al-N coatings, *Scripta Mater.* 113 (2016) 75–78, <https://doi.org/10.1016/j.scriptamat.2015.09.040>.
- [30] M.J. Mehl, D. Finkenstadt, C. Dane, G.L. Hart, S. Curtarolo, Finding the stable structures of $N_{1-x}W_x$ with an ab initio high-throughput approach, *Physical Review B - Condensed Matter and Materials Physics* 91 (18) (2015) 1–19, <https://doi.org/10.1103/PhysRevB.91.184110>.
- [31] K. Balasubramanian, S. Khare, D. Gall, Vacancy-induced mechanical stabilization of cubic tungsten nitride, *Physical Review B* 94 (17) (2016) 36–38, <https://doi.org/10.1103/PhysRevB.94.174111>.
- [32] F. Bachmann, R. Hielscher, H. Schaeben, Texture analysis with MTEX- Free and open source software toolbox, *Solid State Phenom.* 160 (2010) 63–68, <https://doi.org/10.4028/www.scientific.net/SSP.160.63>.
- [33] W. Oliver, G. Pharr, An improved technique for determining hardness and elastic modulus using load and displacement sensing indentation experiments, *J. Mater. Res.* 7 (6) (1992) 1564–1583, <https://doi.org/10.1557/jmr.1992.1564>.
- [34] L. Stöber, J.P. Konrath, V. Haberl, F. Patocka, M. Schneider, U. Schmid, Nitrogen incorporation in sputter deposited molybdenum nitride thin films, *Journal of Vacuum Science & Technology A: Vacuum, Surfaces, and Films* 34 (2) (2016) 021513, <https://doi.org/10.1116/1.4941141>.
- [35] A.A. Bagdasaryan, A.V. Pshyk, L.E. Coy, P. Konarski, M. Misnik, V.I. Ivashchenko, M. Kempniński, N.R. Mediukh, A.D. Pogrebnyak, V.M. Beresnev, S. Jurga, A new type of (TiZrNbTaHfN)/MoN nanocomposite coating: Microstructure and properties depending on energy of incident ions, *Composites Part B: Engineering* 146 (March) (2018) 132–144, <https://doi.org/10.1016/j.compositesb.2018.04.015>.
- [36] C. Stampfl, A.J. Freeman, Metallic to insulating nature of (formula presented) Role of Ta and N vacancies, *Physical Review B - Condensed Matter and Materials Physics* 67 (6) (2003) 1–7, <https://doi.org/10.1103/PhysRevB.67.064108>.
- [37] H. Yusa, F. Kawamura, T. Taniguchi, N. Hirao, Y. Ohishi, T. Kikegawa, High-pressure synthesis and compressive behavior of tantalum nitrides, *J. Appl. Phys.* 115 (10) (2014) 103520, <https://doi.org/10.1063/1.4867986>.
- [38] L. Skala, P. Capkova, Nitrogen vacancy and chemical bonding in substoichiometric vanadium nitride, *J. Phys.: Condens. Matter* 2 (42) (1990) 8293–8301, <https://doi.org/10.1088/0953-8984/2/42/007>.
- [39] A.A. Bagdasaryan, A.V. Pshyk, L.E. Coy, M. Kempniński, A.D. Pogrebnyak, V.M. Beresnev, S. Jurga, Structural and mechanical characterization of (TiZrNbHfTa)N/WN multilayered nitride coatings, *Mater. Lett.* 229 (2018) 364–367, <https://doi.org/10.1016/j.matlet.2018.07.048>.
- [40] J. Buchinger, N. Koutná, Z. Chen, Z. Zhang, P.H. Mayrhofer, D. Holec, M. Bartosik, Toughness enhancement in TiN/WN superlattice thin films, *Acta Mater.* 172 (2019) 18–29, <https://doi.org/10.1016/j.actamat.2019.04.028>.
- [41] J.E. Lowther, Lattice model for the properties of non-stoichiometric cubic and hexagonal molybdenum nitride, *J. Alloy. Compd.* 364 (1–2) (2004) 13–16, [https://doi.org/10.1016/S0925-8388\(03\)00537-1](https://doi.org/10.1016/S0925-8388(03)00537-1).
- [42] F.F. Klimashin, N. Koutná, H. Euchner, D. Holec, P.H. Mayrhofer, The impact of nitrogen content and vacancies on structure and mechanical properties of Mo-N thin films, *J. Appl. Phys.* 120 (18) (2016) 185301, <https://doi.org/10.1063/1.4966664>.
- [43] M. Grumski, P.P. Dholabhai, J.B. Adams, Ab initio study of the stable phases of 1:1 tantalum nitride, *Acta Mater.* 61 (10) (2013) 3799–3807, <https://doi.org/10.1016/j.actamat.2013.03.018>.
- [44] B. Ozsdolay, C. Mulligan, K. Balasubramanian, L. Huang, S. Khare, D. Gall, Cubic β -WN_x layers: Growth and properties vs N-to-W ratio, *Surf. Coat. Technol.* 304 (2016) 98–107, <https://doi.org/10.1016/j.surfcoat.2016.06.079>.
- [45] S. Šsbrink, L. Kihlberg, M. Malinowski, High-pressure single-crystal X-ray diffraction studies of MoO₃. I. Lattice parameters up to 7.4 GPa, *J. Appl. Crystallogr.* 21 (6) (1988) 960–962, <https://doi.org/10.1107/S0021889888008271>.
- [46] Y. Syono, M. Kikuchi, T. Goto, K. Fukuoka, Formation of rutile-type Ta(IV)O₂ by shock reduction and cation-deficient Ta_{0.8}O₂ by subsequent oxidation, *J. Solid State Chem.* 50 (2) (1983) 133–137, [https://doi.org/10.1016/0022-4596\(83\)90180-9](https://doi.org/10.1016/0022-4596(83)90180-9).
- [47] K.D. Rogers, An X-ray diffraction study of semiconductor and metallic vanadium dioxide, *Powder Diffraction* 8 (4) (1993) 240–244, <https://doi.org/10.1017/S0885715600019448>.
- [48] D.J. Palmer, P.G. Dickens, Tungsten dioxide: structure refinement by powder neutron diffraction, *Acta Crystallographica Section B Structural Crystallography and Crystal Chemistry* 35 (9) (1979) 2199–2201, <https://doi.org/10.1107/s0567740879008785>.
- [49] S. Veprek, S. Reiprich, A concept for the design of novel superhard coatings, *Thin Solid Films* 268 (1–2) (1995) 64–71, [https://doi.org/10.1016/0040-6090\(95\)06695-0](https://doi.org/10.1016/0040-6090(95)06695-0).
- [50] R. Chen, G. Qin, H. Zheng, L. Wang, Y. Su, Y.L. Chiu, H. Ding, J. Guo, H. Fu, Composition design of high entropy alloys using the valence electron concentration to balance strength and ductility, *Acta Mater.* 144 (2018) 129–137, <https://doi.org/10.1016/j.actamat.2017.10.058>.
- [51] K. Balasubramanian, S.V. Khare, D. Gall, Valence electron concentration as an indicator for mechanical properties in rocksalt structure nitrides, carbides and carbonitrides, *Acta Mater.* 152 (2018) 175–185, <https://doi.org/10.1016/j.actamat.2018.04.033>.